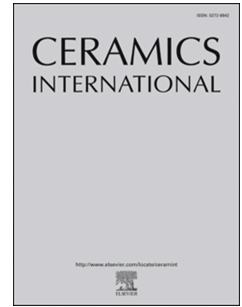


# Journal Pre-proof

Estimation of thermal barrier coating fracture toughness using integrated computational materials engineering

Xibo Geng, Richard Wellman, Luis Isern Arrom, Christine Chalk, Gustavo Castelluccio



PII: S0272-8842(23)01382-2

DOI: <https://doi.org/10.1016/j.ceramint.2023.05.124>

Reference: CERI 36653

To appear in: *Ceramics International*

Received Date: 13 February 2023

Revised Date: 9 May 2023

Accepted Date: 14 May 2023

Please cite this article as: X. Geng, R. Wellman, L.I. Arrom, C. Chalk, G. Castelluccio, Estimation of thermal barrier coating fracture toughness using integrated computational materials engineering, *Ceramics International* (2023), doi: <https://doi.org/10.1016/j.ceramint.2023.05.124>.

This is a PDF file of an article that has undergone enhancements after acceptance, such as the addition of a cover page and metadata, and formatting for readability, but it is not yet the definitive version of record. This version will undergo additional copyediting, typesetting and review before it is published in its final form, but we are providing this version to give early visibility of the article. Please note that, during the production process, errors may be discovered which could affect the content, and all legal disclaimers that apply to the journal pertain.

© 2023 Published by Elsevier Ltd.

# Estimation of Thermal Barrier Coating Fracture Toughness Using Integrated Computational Materials Engineering

Xibo Geng<sup>1,2</sup>, Richard Wellman<sup>3</sup>, Luis Isern Arrom<sup>1</sup>, Christine Chalk<sup>1</sup>, Gustavo Castelluccio<sup>1\*</sup>

<sup>1</sup> School of Aerospace, Transport and Manufacturing, Cranfield University, Bedfordshire, UK

<sup>2</sup> Siemens, UK

<sup>3</sup> Innio, Jenbach, Austria

## Abstract

The fracture toughness of thermal barrier coatings (TBC) is a critical mechanical property that governs damage resistance. Catastrophic delamination of TBC under erosion conditions occurs in TBC with low toughness. Prior research has explored indirect and complex experiments to measure TBC toughness, but the miniaturized nature of the multi-layered coating makes it difficult to quantify its intrinsic toughness. This paper integrates computational modeling and experimental approaches to estimate the TBC toughness and the substrate delamination strength. The results show that a typical newly fabricated yttrium stabilized zirconia coating under service conditions has a toughness estimated in the range of 0.1 to 0.5 MPa·m<sup>1/2</sup> and a toughness of thermally grown oxide layer in between 1.5 to 1.7 MPa·m<sup>1/2</sup>. The analysis also determined that a thermally grown oxide with a fracture toughness above 2.0 MPa·m<sup>1/2</sup> would not delaminate under the service conditions. Overall, the approach demonstrates the value of integrated computational material approaches, which can save time and enhance predictive power.

## Keywords:

EB-PVD TBC, Foreign object damage, Ceramic fracture toughness, TBC fracture mechanics, Finite Element Analysis, TBC kink-bands, and Alumina interface fracture

## Introduction

Aeroengine manufacturers require modern gas turbines to operate at increasingly higher temperatures to reduce CO<sub>2</sub> emissions and achieve better fuel efficiency. Thermal Barrier Coatings (TBCs) (Figure 1 a) are a critical material solution that offers thermal insulation in the hottest engine sections, allowing them to work at higher temperatures and for a longer lifespan. A typical TBC system consists of three layers as shown in Figure 1 b). A ceramic Top Coat (TC), an active Thermally Grown Oxide (TGO) layer that thickens with the engine aging, and a metallic Bond Coat (BC). TCs are normally manufactured using Electron Beam Physical Vapour Deposition (EB-PVD) on rotating turbine components such as the high-pressure turbine blade in Figure 1 a). Ceramic structures are separated by inter-columnar gaps and feathery structures that result from secondary grain growth (Figure 2). Columnar TBCs offer high damage tolerance, which is required by high thermal cyclic applications [1].

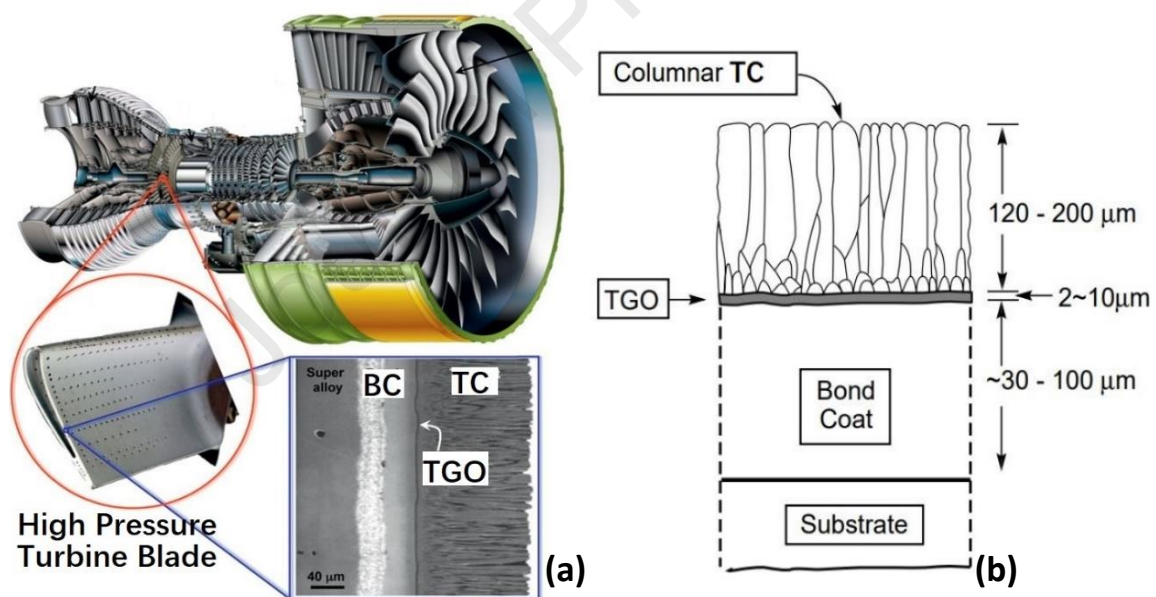


Figure 1 (a) Turbine blade in aero-engine cutaway and TBC SEM image, (b) EB-PVD TBC schematic with thickness ranges of each layer [2] [3].

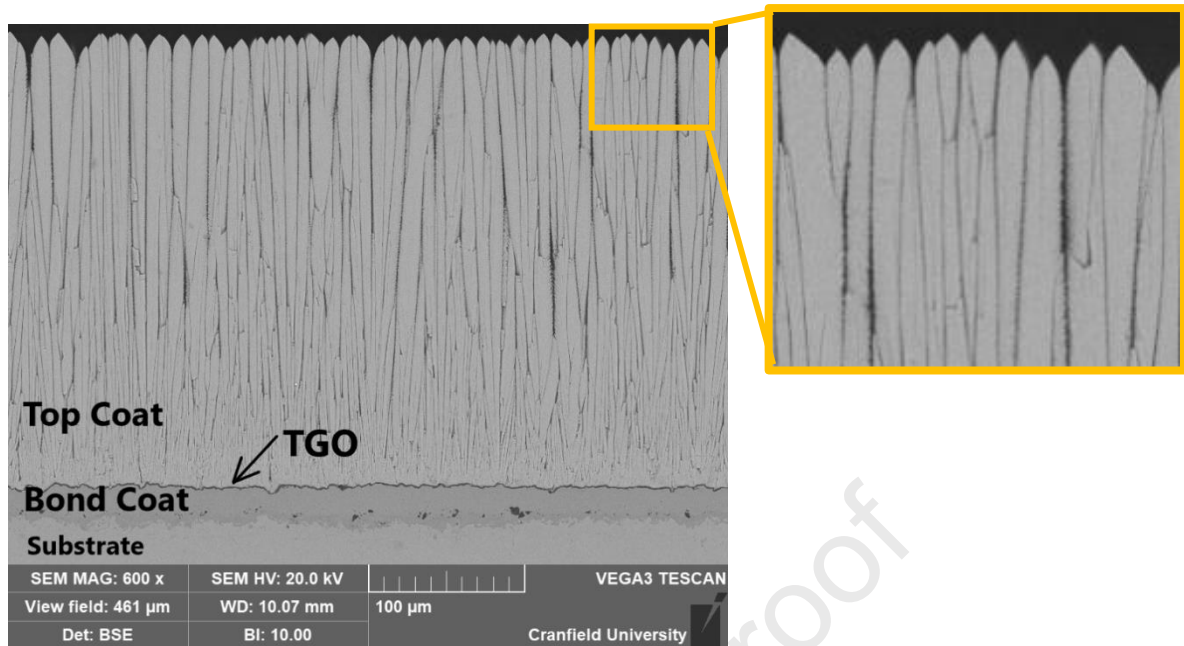


Figure 2. SEM image of TBC cross-section and zoomed view of the top coat column's feathery edges shown in the yellow circle.

During service, TBCs are subjected to chemical degradation (e.g., oxidation, corrosion, etc) and mechanical erosion from the impact of airborne particles ingested by the engine. Currently, industry standard TBC corresponds to 7wt% yttrium stabilized zirconia (7YSZ) [1] and attempts to introduce new materials resulted in poor erosion resistance due to the apparent lower fracture toughness [4][5][6]. Therefore, identifying TBC toughness becomes a critical aspect to ascertain erosion resistance and predict TBC service life in an erosive environment.

The small thickness of TBCs and the heterogeneity of their structure prevent the implementation of standardized fracture toughness testing. Hence, TBC toughness has often been indirectly estimated by indentation methods [7], which are time-consuming, ambiguous, and sometimes unavailable (e.g., at high temperatures and high deformation rates). Indeed, prior approaches rely on multiple assumptions to justify a closed correlation among observable quantities (local stress, penetration depth, and energy applied) with toughness. As a result, toughness estimation may be unreliable and may have significant uncertainty, especially when extrapolated to service conditions.

Prior computational efforts [8][9] have compared the response of TBC with experiments to study different material and microstructural effects during thermal

cycling. However, only a few approaches have focused on structure-sensitive approaches capable of estimating the coating toughness. Hence, we present substructure-sensitive finite element simulations (FEM) with columnar multi-layered microstructure to quantify TBC toughness by comparing simulation results with foreign object damage (FOD) experimental observations. This approach identifies various observable indicators that are employed to characterize toughness and delamination resistance at high temperatures and high strain rates. The results present a novel solution to estimate the mechanical response of TBCs under realistic service conditions.

### Experimental characterization

TBC samples were fabricated on a 1.6 mm thick Nimonic 75 substrate with a NiAl bond coat deposited by Chemical Vapour Deposition and a top coat of 7YSZ deposited by EB-PVD using a Von Ardenne EBE150 system. Samples were tested in an erosion rig schematically depicted in Figure 3, which simulates FOD from millimeter-sized particles impacting turbine blades TBC at speeds above 100 m/s [10][11]. The rig directs hot gas at 1000°C towards samples to reach typical TBC service temperatures of 800~880°C. A total of 0.1g Honite particles with a diameter between 700  $\mu\text{m}$  to 850  $\mu\text{m}$  were added to the airstream to impact the TBC sample at high speed. Prior experimental efforts [12][13] have demonstrated that this method results in damage mechanisms and extensions similar to those suffered by turbine engines during service. Moreover, the rig allows one to measure and control precisely the environment at a fraction of the cost of running a real engine.

Figure 4 exemplifies the damage induced by the erosion rig on a TBC sample. Figure 4 a) corresponds to the top view of the TBC while Figure 4 b) presents a scanning electronic microscopy (SEM) image of the sample cross-section, which was cut and polished along the highlighted line. The average impact penetration depth ( $\delta_{\text{max}}$  in Figure 4 b) measured from cross-section images is a key damage indicator of TBC FOD as shown in previous studies [14][15][16][17].

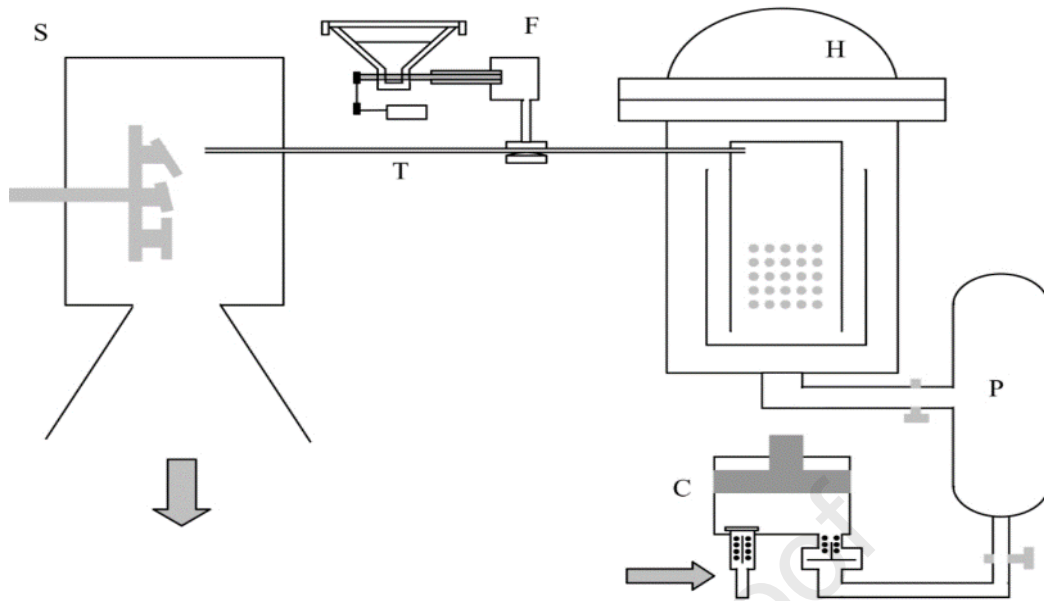


Figure 3. Schematics of erosion rig – furnace (H), gas tube (T) connecting furnace and TBC sample chamber (S), erosion particle feeding device (F) [11][18].

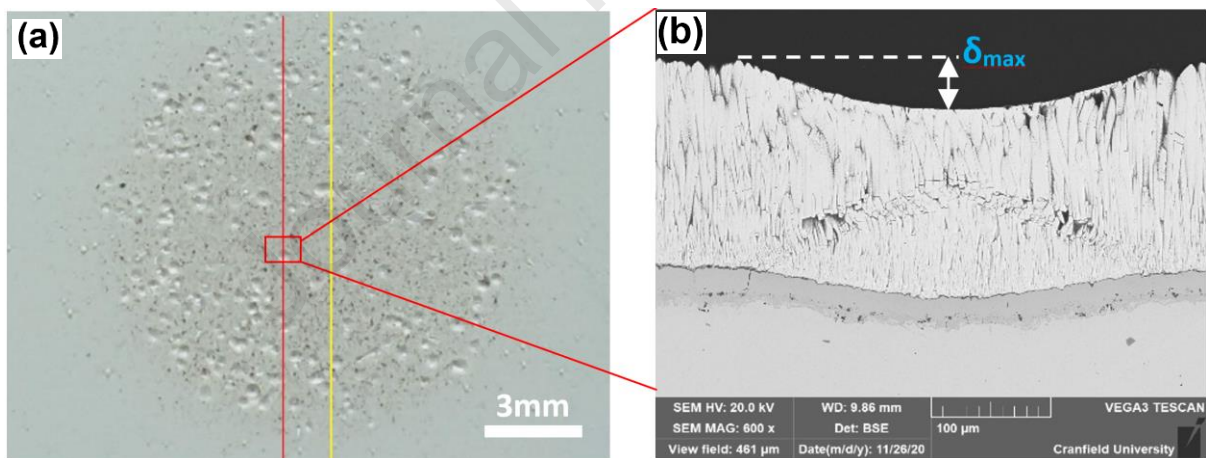


Figure 4. (a) Top-view of a damaged TBC sample with yellow cut line and red polish line, (b) SEM image of TBC cross-section under crater at the highlighted red area, note the kink-band on the TBC.

### Modeling approach

FEM models in Abaqus/CAE 2022 were implemented to conduct Dynamic/Explicit analysis that simulates the FOD impact on TBC. The models shown in Figure 5 consist of a 1 mm thick substrate covered with three layers: TC, TGO, and BC with a thickness

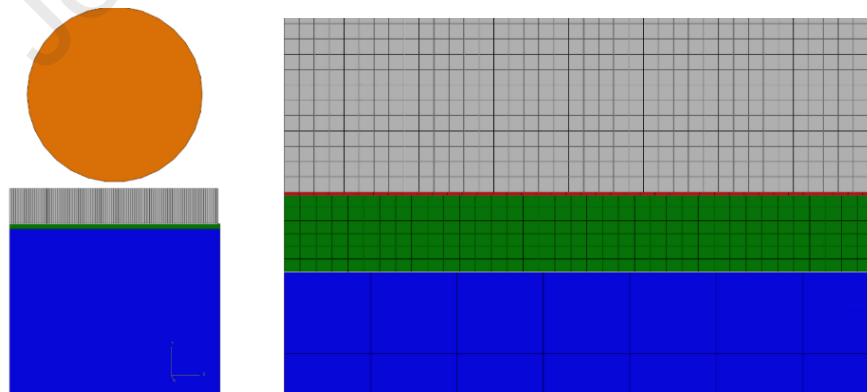


of 170  $\mu\text{m}$ , 1  $\mu\text{m}$ , and 25  $\mu\text{m}$ , respectively; the TGO thickness corresponds to a pristine coating that has not been aged. Experiments [14][15] suggest that FOD results in an affected area with a typical radius of 350  $\mu\text{m}$ . Therefore, the TBC model employs a sample side length of 1mm as shown in Figure 5. Furthermore, the FOD particle corresponds to a rigid ball 850  $\mu\text{m}$  in diameter and an impact speed of 100  $\text{ms}^{-1}$ , which agrees with experiments to model the expected highest velocity.

Both 2D and 3D models depict a simplified TC composed of columnar beams with a 1  $\mu\text{m}$  inter-columnar gap. The 2D model in Figure 5 (a) employs quadratic elements to represent rectangular 10  $\mu\text{m}$  columnar TC and continuous TGO with a mesh size of 5  $\mu\text{m}$ , while the BC and the substrate have 4  $\mu\text{m}$  and 25  $\mu\text{m}$  mesh size, respectively. Both models have the same boundary conditions, in which the TBC is fixed at the substrate bottom and pinned supported at the edges of the modeled sample.

The 3D model in Figure 5 (b) employs a mesh size of 6.8  $\mu\text{m}$  for the columnar TC and TGO, 12.5  $\mu\text{m}$  for the BC, and 25  $\mu\text{m}$  for the substrate. The TC corresponds to a 3D array of square-shaped cross-section columns with a constant inter-columnar gap. Compared to the TBC microstructure in Figure 2, feather arms and intra-columnar porosity have not been explicitly represented in the models for simplification. Instead, a Coulomb friction model captures intercolumnar and top surface-ball interactions.

a)



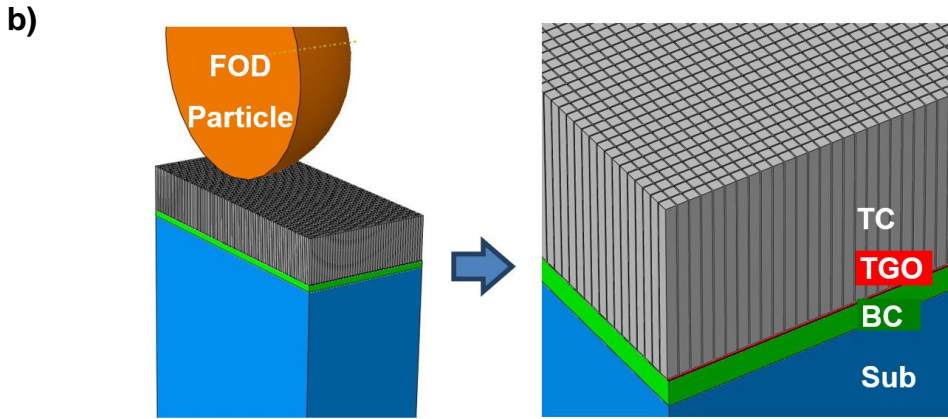


Figure 5. FEM models represent a foreign object impacting a TBC with three layers. (a) 2D model, (b) 3D model. Note both the 2D and 3D models have employed the array of continuous columns to represent the EB-PVD TBC columnar microstructure.

### Material attributes

Much of the inelastic response of TBCs comes from the progressive compactification of the TC, which lacks significant strain hardening mechanisms. Hence, we proceed by approximating the TC response as an elastic-perfectly plastic response, which has often been used to represent compactification [19][20]. This model corresponds to a linear elastic response up to the yield stress, after which the stress remains constant with further straining. As demonstrated by Matsuzawa et al. [21], the yield stress of 7YSZ ceramics ( $\sigma_Y$ ) is strain-rate dependent. Given that experiments [14] have shown that TC and BC experience strain rates of about  $10^6 \text{ s}^{-1}$  around the impact crater, the models should convey strain-rate effects. Hence, we employ a yield stress constitutive model with a power law dependence [14][22] on the strain rate,

$$\sigma_Y(\dot{\varepsilon}) = \sigma_Y(0) \left[ 1 + \left( \frac{\dot{\varepsilon}}{C} \right)^{\frac{1}{P}} \right] \quad (1)$$

in which  $\sigma_Y(0)$  is the quasistatic yield stress,  $\dot{\varepsilon}$  corresponds to the instantaneous strain rate while  $C$  and  $P$  are material parameters related to the Johnson-Cook rate dependence model [23]. The unavailability of high strain-rate related data for zirconia makes it difficult to precisely calibrate the material yield stress at a high strain rate. Instead, we mimic the response of AlN ceramics [24], for which the dynamic yield stress is approximately three times its quasi-static yield stress. Thus, as a first-order



approximation we assume that zirconia has a similar response to AlN ceramics and we employed a multiplication factor of three to characterize TC and BC yield stresses at a high strain rate.

During FOD experiments, the sample temperature is on average at 840°C, at which the fracture stress of TGO ( $\sigma_{\text{Debonding}}$ ) is approximately 100 MPa according to the fracture map of alumina [25]. By further assuming that a strain rate multiplication factor of three applies to  $\sigma_{\text{Debonding}}$ , we estimate the fracture stress of alumina under testing conditions to be approximately 300 MPa [6].

The FOD particle is modeled as an elastic ball that does not break during impact. Given the lack of data, the yield stress of the TGO is approximated by that of the TC without any significant effect due to the relatively small thickness of the TGO. Table 1 presents the material properties, which were estimated from experimental data at high temperatures. We highlight that we will proceed with the analysis assuming these are independent parameterizations and we will perform a sensitivity analysis rather than calibrating the parameters to match exactly our experimental results.

Table 1 TBC model material characterisations [14][26][27][28][29][30]

	Material	Density (kg/m <sup>3</sup> )	Young's modulus (GPa)	Poisson's ratio	Yield stress (MPa)	Strain-rate dependent yield stress (MPa)
FOD Particle	Honite at room temp	1500	72	0.23	N/A	N/A
TC	7YSZ at 900°C	5900	62	0.25	180	X3 =540
TGO	Alumina at 800°C	3500	325	0.25	180	540
BC	NiAl at 800°C	5900	110	0.31	120	X3 =360
Substrate	Nimonic 75 at 800°C	8360	165	0.3	190	N/A

## TGO cohesive contact

The delamination between the TGO and the BC is evaluated with a cohesive contact model shown in Figure 6 a). The cohesive contact model is defined by the traction-separation law in Figure 6 b) [8], which is characterized by the three parameters: elastic behavior of the cohesive contact represented by modulus ( $K$ ), damage initiation stress level ( $\sigma_{\text{Debonding}}$ ), and fracture energy ( $G_c$ ) defined by the area under the curve. As demonstrated next, we considered an integrated engineering approach that validates these parameters based on the debonded crack length observed on experimental samples.

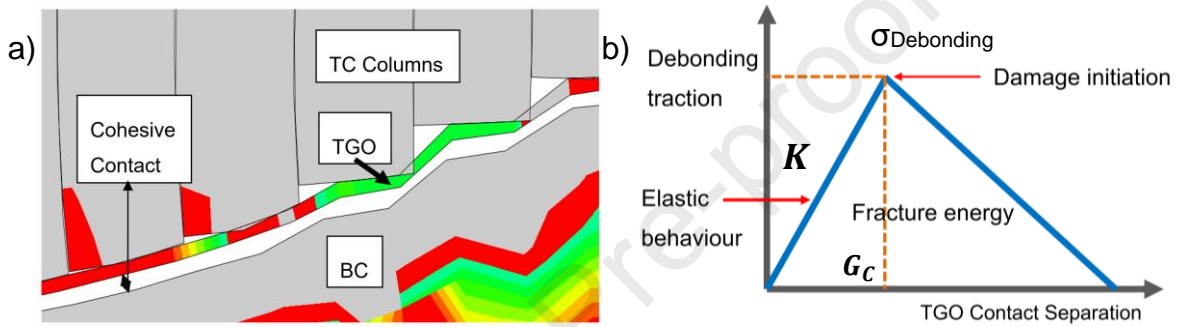


Figure 6. a) 2D Model FOD simulation shows the separation of TC/TGO from BC governed by the cohesive contact applied between TGO and BC. b) Traction-separation law of cohesive contact [8].

## Modeling Results

### Parameter sensitivity analysis

Given the experimental difficulties in identifying material constants, we proceed with a sensitivity analysis running 2D and 3D simulations with small changes to the parameters in Table 1. For each simulation, we quantified the impact penetration depth, which is a useful indicator of FOD damage. Figure 7 presents the penetration depth ( $\delta$ ) calculated with 2D models using ranges for the values of the TC density ( $\rho^{\text{TC}}$ ), Young's modulus ( $E^{\text{TC}}$ ), Poisson's ratio ( $\nu^{\text{TC}}$ ), static yield stress ( $\sigma_Y^{\text{TC}}$ ), thickness ( $h^{\text{TC}}$ ), inter-columnar gap ( $g$ ), friction coefficient of the top TC surface ( $\mu_P$ ) and friction coefficient of the column edge surface ( $\mu_C$ ). The results in Figure 8 demonstrate that density and elastic properties have a minimal effect on the FOD penetration depth; hence, the role of the feather crystal orientation in affecting FOD is secondary. The

column edge friction coefficient and the inter-columnar gap affect the penetration by about 10% to 30%, respectively, which agrees with the results by Wang et al. [7] despite assuming a bilinear kinematic hardening model. Finally, the yield stress affects the most penetration prognosis, but an increase in yield strength of 500% only changes the penetration by 40%.

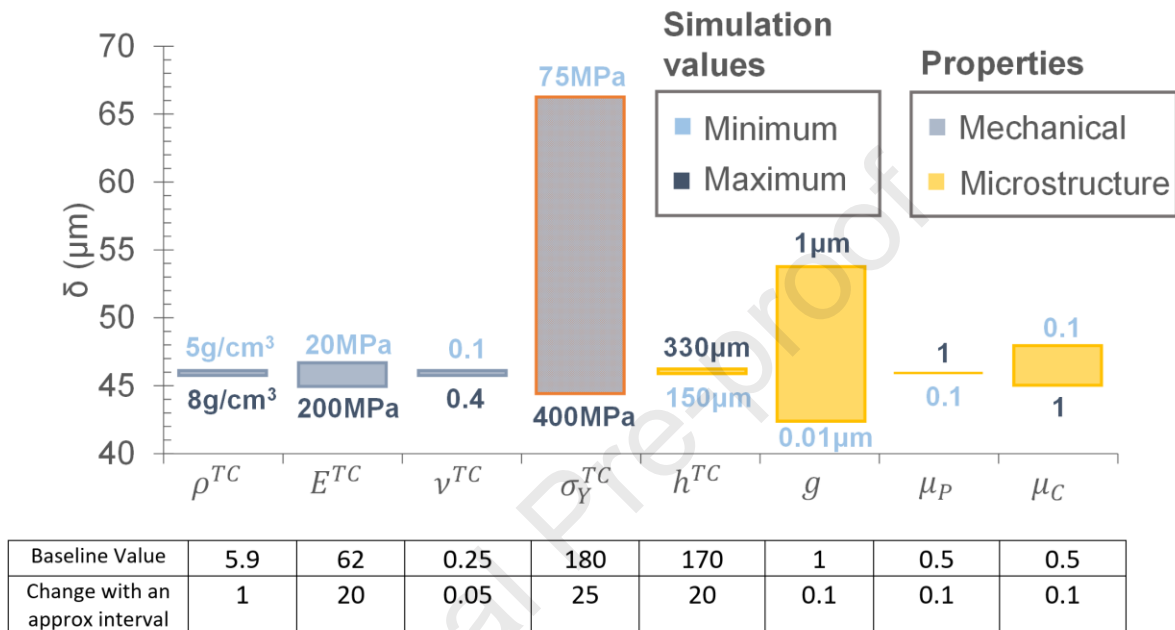


Figure 7. Effects of each TC property on FOD penetration depth ( $\delta$ ) quantified with the 2D model sensitivity tests with FOD particle of 850  $\mu\text{m}$  diameter impacting at 100m/s. Properties changed one at a time within an interval of change noted in blue.

Next, we considered the sensitivity to particle diameters between 700 and 850  $\mu\text{m}$  and impact velocity between 50 to 100 m/s at 900°C. In this case, we employ inter-columnar gaps of 1  $\mu\text{m}$  and a static yield stress of TC is 180 MPa with a multiplication factor of three for the strain-rate-dependence. Figure 7 summarizes the FOD penetration depths from five experimental samples using 2D and 3D models. These results show a surprisingly close match between models and experiments, even when considering independent best estimates for some material properties. Thus, model input uncertainty is not detrimental enough to affect the model predictive power of the penetration depth, which is related to kink bands and delamination inside TBC [14][15][16][17].

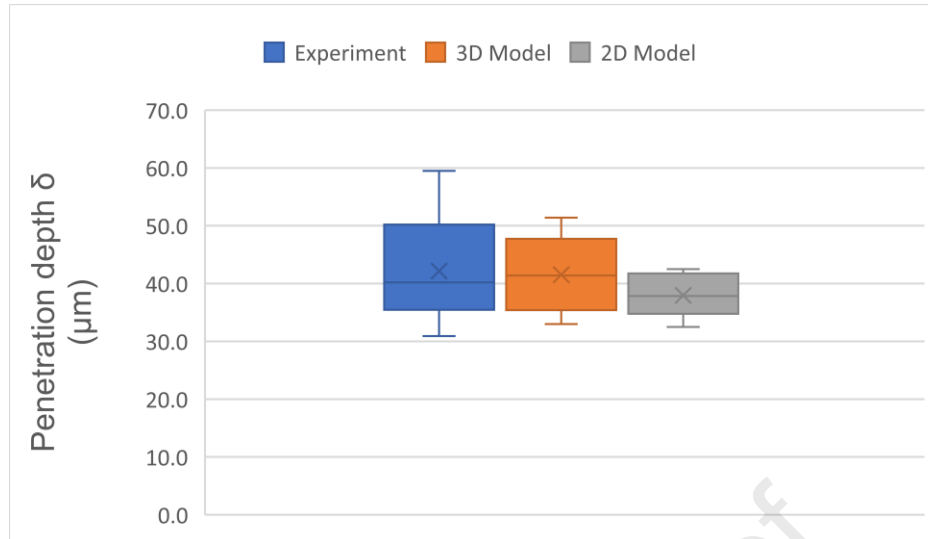


Figure 8. Effects of Honite particle diameter (700~850  $\mu\text{m}$ ) and speed (50~100 m/s) on FOD penetration depth ( $\delta$ ) compared between experiment samples, 2D and 3D FEM models, showing a close match

### Kink bands and crack indicators

Given the brittle nature of TBC, the maximum principal stress is a natural damage indicator parameter for the potential of crack initiation. Indeed, the red stress concentrated zones shown in Figure 9 closely resemble the experimental kink bands in Figure 4. The kink-band-like field corresponds to tensile stresses that arise from the bending of the columns and highlight the value of representing the TBC substructure. The results present a compactification zone right under the impact point, continued by a kink band with a chevron pattern in the range of 45~90 MPa for a 2D model.

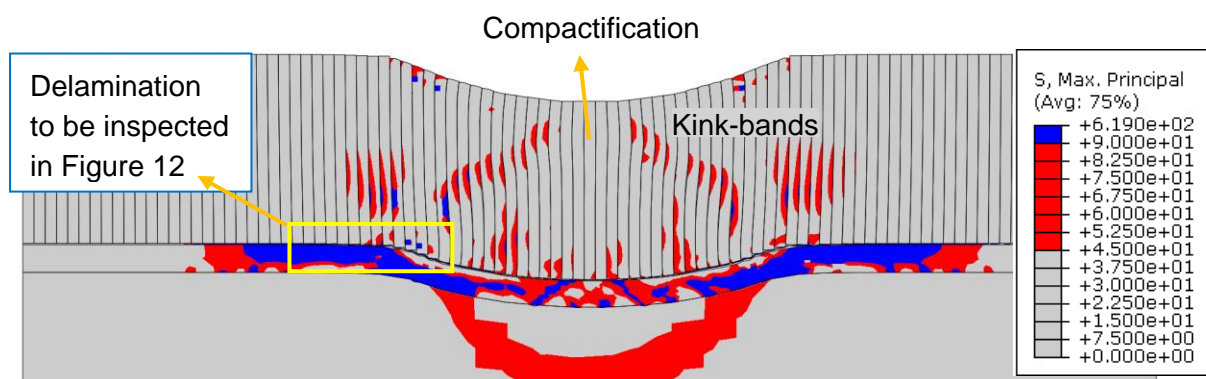


Figure 9. Maximum principal stress computed with a 2D model of TBC after the impact of a spherical rigid particle with a diameter of 850  $\mu\text{m}$  and speed of 100 m/s (units in MPa)

Figure 10 a) depicts the 3D model along with SEM images from a FOD experiment sample. Both models and experiments develop similar compaction zones underneath the top surface around the impact center, which gradually reduces as the cross-section moves away from the center. At the cross-section in the medium point between the impact center and the crater edge (Figure 10b), there is no compaction, but cracks have developed underneath the top surface in the middle area. These cracks correlate with the location of the maximum principal stresses in TC (60 to 90 MPa), which is taken as the critical stress to crack the column. The maximum principal stress depicts a chevron crack pattern (kink-band) from the bending of the columns. Notably, for similar impact speed, columns in 3D models become less bent compared to bending in 2D.

At the impact center and the medium position in Figure 10a/b, severe cracking occurs at kink bands. SEM images show the kink bands start from the middle of the TC and propagate towards the TGO. The 3D model shows similar patterns by painting red elements with principal stress between 60 and 90 MPa. In Figure 10, cracks near the crater boundary are also found in the SEM image. These cracks are not as open as in the kink bands and they are around the circular crater boundary near the top surface. The 3D model also shows several red elements with local principal stresses in the range of 60 to 90 MPa around the circular crater boundary in Figure 10.

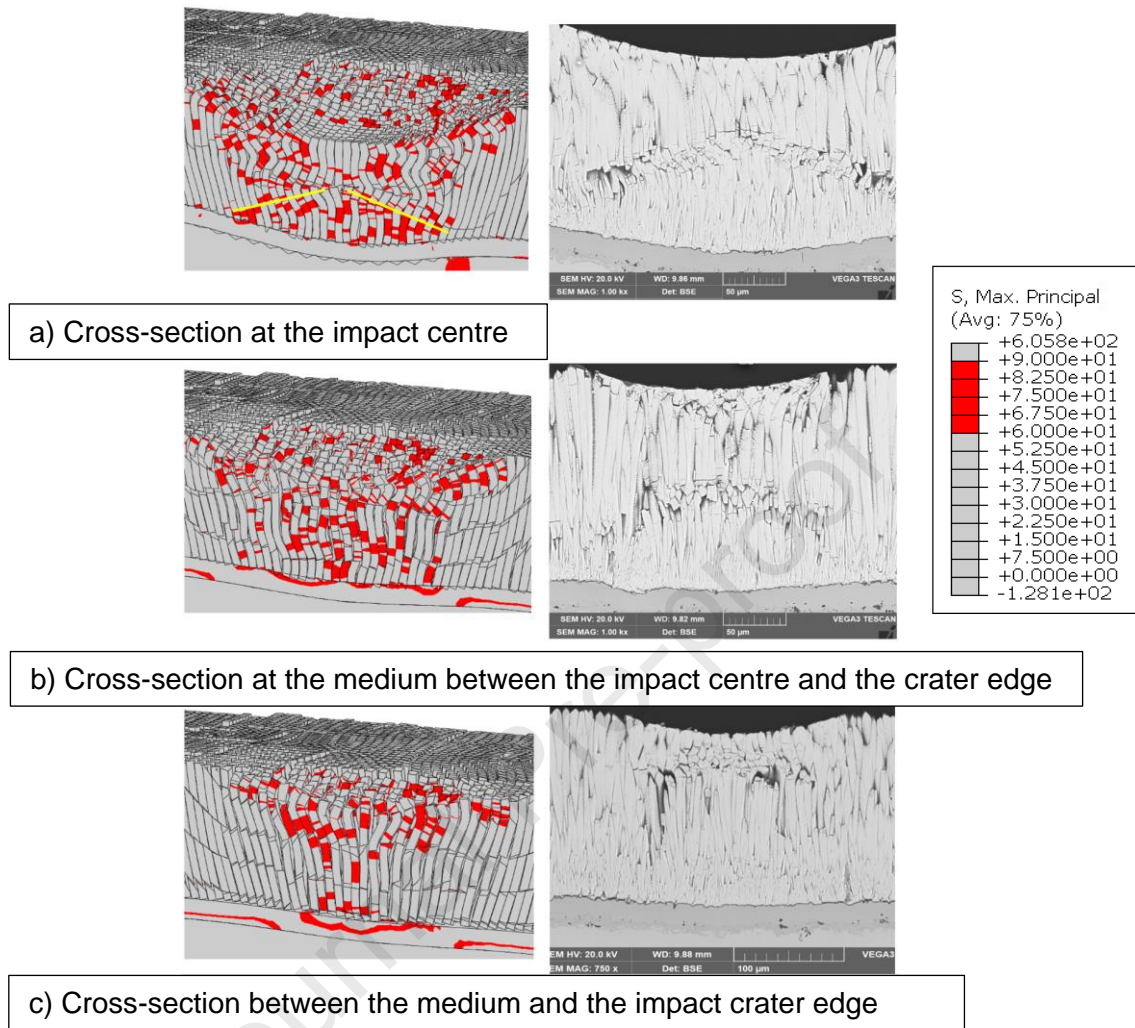


Figure 10. Comparisons of 3D model prediction with experimental SEM image of the three cross-sections located across the impact crater

### Estimation of TGO interface delamination fracture energy

Our sensitivity analysis shows that simple material models and independent estimations of material properties carry good intrinsic predictive power for particle penetration and kink band formation. Indeed, several researchers have modeled particle penetration and supported the use of simple models to quantify complex attributes such as fracture toughness and delamination [31].

The cohesive contact model between TGO and BC is governed by the three parameters,  $K$ ,  $G_c$ , and  $\sigma_{\text{Debonding}}$  as defined in Figure 6 b). Since the TGO is a thin



(1 $\mu\text{m}$ ) layer formed by alumina ( $\alpha\text{-Al}_2\text{O}_3$ ), the elastic behavior of TGO is governed by Young's modulus of TC, which is estimated to be 62 GPa at 900°C [28]. The peak (debonding) stress  $\sigma_{\text{Debonding}}$  is about 100 MPa according to the transcrystalline cleavage fracture stress of alumina at 800°C [25]. After inspecting the sample, the longest TGO delamination crack length is approximately 120  $\mu\text{m}$ , as shown in Figure 11.

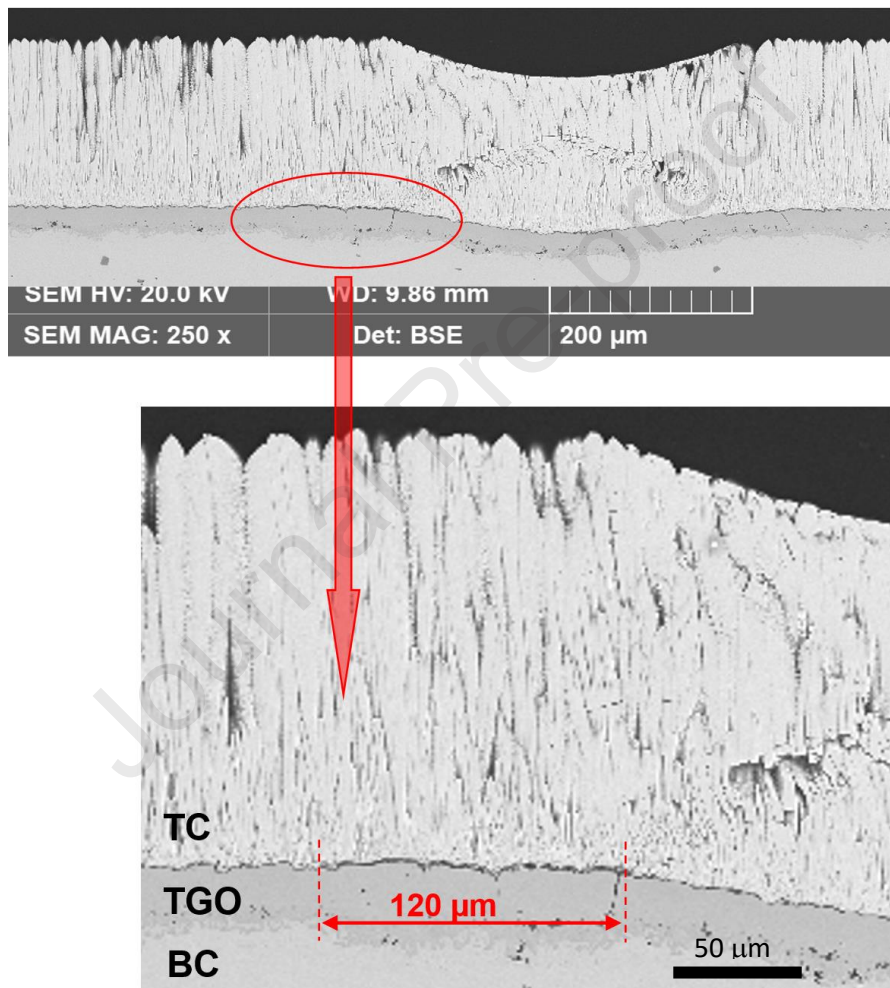


Figure 11. Experiment measurement of the maximum length of delamination occurred at the TC/TGO or TGO/BC interfaces at one side of the TBC.

We can estimate the fracture energy by assuming that the longest delamination crack was caused by a ball with the largest diameter (850  $\mu\text{m}$ ) traveling at the fastest speed (100 m/s). Hence, we performed a sensitivity study with the 2D model, assuming a

range of fracture energies and computing the corresponding TGO interface delamination length as shown in Figure 12. The results in Figure 13 demonstrate that a decrease in fracture energy increases the delamination crack length. The experimental observation in Figure 11 with a 120  $\mu\text{m}$  crack corresponds to a fracture energy  $G$  between 35  $\text{Jm}^{-2}$  to 45  $\text{Jm}^{-2}$  as shown in Figure 13. These results agree with prior reports [7], which estimated the fracture energy to be about 20  $\text{Jm}^{-2}$  to 38  $\text{Jm}^{-2}$  for TBC samples after 35 thermal cycles. Since our samples were newly fabricated and had not been aged, we would expect their fracture energy to be higher.

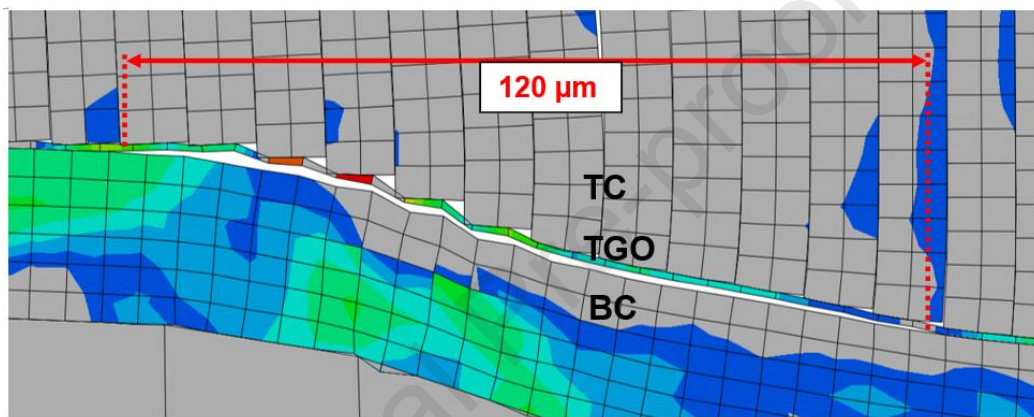


Figure 12. Detail of the simulated delamination crack matching the experimental results in Figure 9. The results suggest that the fracture energy  $G$  is between 35  $\text{Jm}^{-2}$  to 45  $\text{Jm}^{-2}$

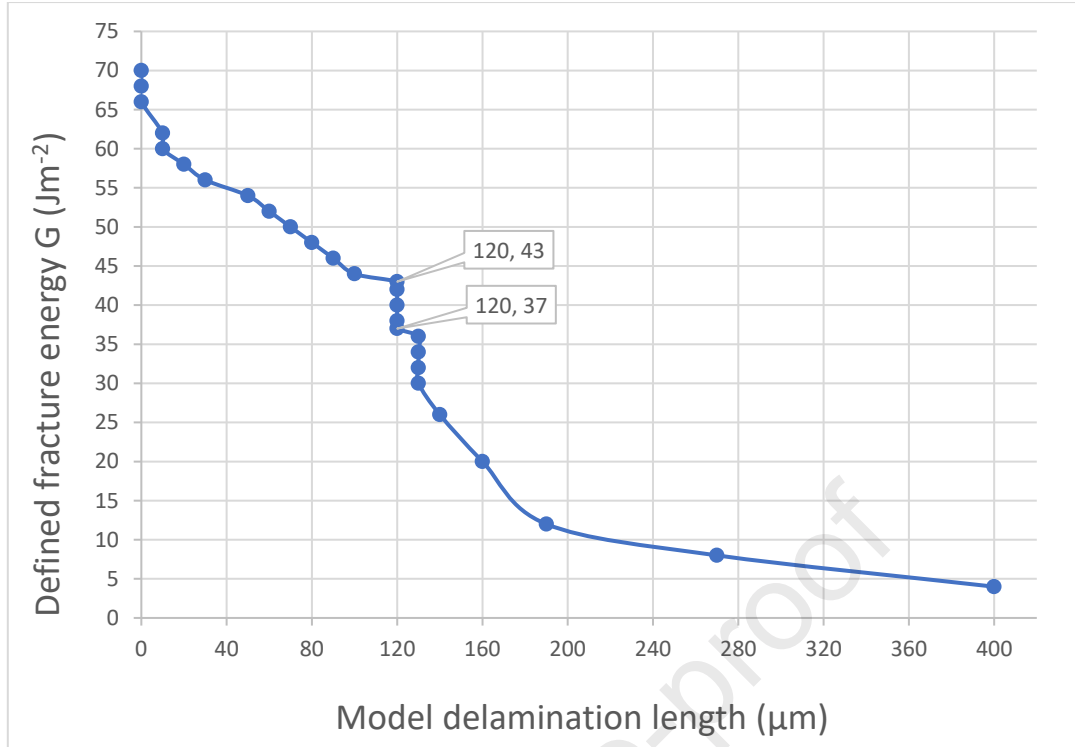


Figure 13. TBC delamination length (on one side) predicted by the 2D model with different fracture energies ( $G$ ), different values of  $G$  can result in the same delamination length because of the discrete nature of the mesh

### Kink-bands crack analysis and TC fracture toughness

The simulations suggest that the minimum crack initiation tensile stress is 45 MPa and 60 MPa for 2D and 3D models, respectively. Hence, we can estimate the tensile stress required to fracture the TC is in the range of 45 to 90 MPa. Following linear elastic fracture mechanics, the critical stress intensity factor ( $K_{IC}$ ) of a sharp crack can be computed by,

$$K_{IC} = \sigma \sqrt{\pi a} f(a/W). \quad (2)$$

Following the critical stress computed with simulations, we assume stress  $\sigma = 45 \sim 90$  MPa, geometry factor  $f(a/W) = 1.122$  [32], and an initial crack length ( $a$ ) between 2~7  $\mu\text{m}$  as measured in Figure 14. The resulting  $K_{IC}$  is between 0.1~0.5  $\text{MPa}\cdot\text{m}^{1/2}$ , which agrees with Evan's estimation of YSZ mode-I fracture toughness between  $0.1 \leq K_{IC} \leq 1$   $\text{MPa}\cdot\text{m}^{1/2}$ [22][28]. Thus, we demonstrate that simulations, FOD experiments, and material characterization can be effectively integrated to identify the crack initiation stress and TC Mode-I fracture toughness.

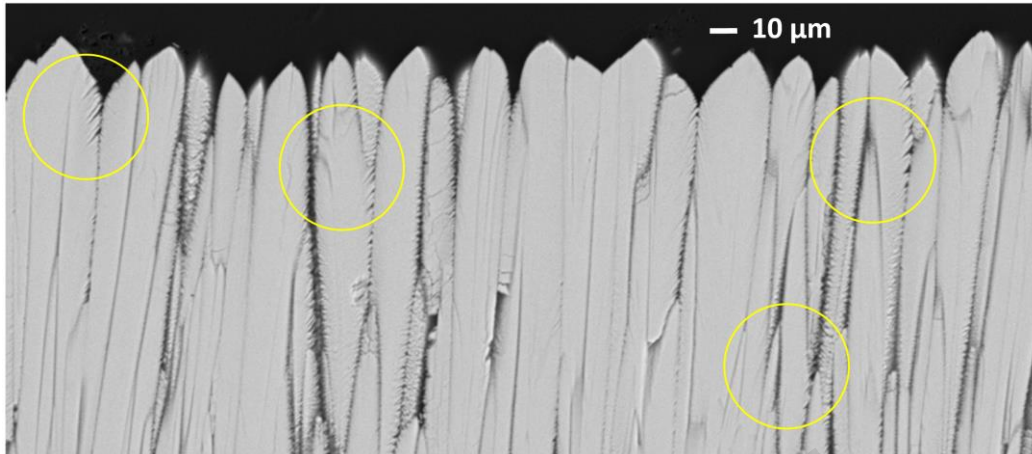


Figure 14. TC SEM image showing the micro-cracks on column edges

### Estimation of the TGO interface fracture toughness

The fracture energy can also be related to the critical stress intensity factor,

$$G_C = (K_{IC})^2/E, \quad (3)$$

along with the TC Young's modulus to compute the critical fracture toughness of the delamination at the alumina interface. Following our calculation of  $G_C$ , the fracture toughness of the TGO alumina interface at 800°C is estimated as  $K_{IC} = 1.5\sim 1.7$  MPa·m<sup>1/2</sup>. The fracture toughness of TGO has not been reported in the existing literature, but measurements of plasma-sprayed alumina coatings using indentation resulted in 0.5 ~ 2.5 MPa·m<sup>1/2</sup> depending on manufacturing routes [33]. By comparison, our estimated range of TGO fracture toughness lies within the experiment-measured range of toughness of alumina coating, thus the estimation can be considered reasonable.

### Discussion

The measurement of mechanical properties in TBCs is a challenging task given their small dimensions and complex microstructures. Rather than solely relying on costly and time-consuming coating indentation experiments, we have presented a blended approach that integrates information from various sources. We implemented finite element models and sensitivity analyses to identify the material properties that most

affect particle penetration and coating delamination. The independent identification of these properties mitigated model input errors while models were further validated by comparing penetration depths and cracking patterns from experiments. Our integrated computational materials engineering approach offers the benefit that the uncertainty of the results can be further characterized and reduced with additional experimental testing and characterization. In addition, by analyzing components used in-service, our approach provides a unique strategy to estimate the mechanical properties under operational conditions.

Figure 13 further demonstrates the potential to integrate the computational approach to the selection and design of materials. A modest increase in fracture energy of the TGO interface to reach  $50 \text{ Jm}^{-2}$  (equivalent to  $1.8 \text{ MPa}\cdot\text{m}^{1/2}$ ) would reduce the delamination length by 50% from  $120 \text{ }\mu\text{m}$  to  $60 \text{ }\mu\text{m}$ . Furthermore, an increase of fracture energy of the TGO interface above  $70 \text{ Jm}^{-2}$  or  $2.0 \text{ MPa}\cdot\text{m}^{1/2}$  would result in no delamination at the alumina interface estimated from Figure 13, and this value can be considered as the optimal fracture toughness value for TBC design.

The TC Young's modulus also plays an important role in interface toughness and a TC bottom layer near the substrate with high Young's modulus is desirable as well for increasing FOD resistance. In this case, a stronger, tougher, and dense YSZ bottom layer in TC would also be helpful to increase the alumina interface toughness. These findings have confirmed the dependence of interface delamination on the alumina fracture stress, energy release rate (fracture energy), and Young's modulus of TC as reported in the existing literature [14][22][28].

## Conclusions

This paper integrates experiments with 2D and 3D finite element models that explicitly represent the microstructure of TBC to simulate the damage induced by the impact of foreign objects. Crack-dependent parameters were adjusted to match crack morphology and length observed in experiments. In this way, material parameters such as fracture stress and energy release rate of the TBC were identified, from which the fracture toughness of TC and alumina interface are calculated.

The analysis estimated material properties independently and assessed model input sensitivities. Best estimates of material parameters informed models to predict localized damage at kink bands and estimate the interface delamination. In terms of the TBC samples, the fracture toughness of TC was estimated to be around 0.1 MPa·m<sup>1/2</sup> to 0.5 MPa·m<sup>1/2</sup> and the fracture toughness of the TGO interface was about 1.5 MPa·m<sup>1/2</sup> to 1.7 MPa·m<sup>1/2</sup>. These ranges derived from models agree with the values reported in the literature for similar materials.

Our analysis also determined that a TGO with a fracture toughness above 2.0 MPa·m<sup>1/2</sup> would not delaminate under the service conditions replicated in the erosion test. This modeling approach can be used to design novel TBC by optimizing microstructure, micro-porosity, column size, inter-column friction, and yield strength.

The novel integrated computational approach of material engineering enables a simple characterization of TBC toughness under service conditions and offers great potential to support the design of novel TBC systems. Compared to the conventional experimental methods, using the integrated approach is also more cost-effective and less time-consuming. The approach can also be employed to design the composition and microstructure of TBCs and advance erosion-resistant systems for next-generation coatings.

## References

1. Wellman RG., Nicholls JR. A review of the erosion of thermal barrier coatings. *Journal of Physics D: Applied Physics*. 2007; 40(16). Available at: DOI:10.1088/0022-3727/40/16/R01
2. Clarke DR., Oechsner M., Pature NP. Thermal-barrier coatings for more efficient gas-turbine engines. *MRS Bulletin*. 2012; 37(10): 891–898. Available at: DOI:10.1557/mrs.2012.232
3. Karlsson AM., Hutchinson JW., Evans AG. A fundamental model of cyclic instabilities in thermal barrier systems. *Journal of the Mechanics and Physics of Solids*. 2002; 50: 1565–1589. Available at: 10.1016/S0022-5096(02)00003-0



4. Watanabe M., Mercer C., Levi CG., Evans AG. A probe for the high-temperature deformation of thermal barrier oxides. *Acta Materialia*. 2004; 52(6): 1479–1487. Available at: DOI:10.1016/j.actamat.2003.11.029
5. Zhu D., Nesbitt JA., Barrett CA., McCue TR., Miller RA. Furnace Cyclic Oxidation Behavior of Multicomponent Low Conductivity Thermal Barrier Coatings. *Journal of Thermal Spray Technology*. 2004; 13(1): 84–92. Available at: DOI:10.1361/10599630418185
6. Frommherz M., Scholz A., Oechsner M., Bakan E., Vaßen R. Gadolinium zirconate/YSZ thermal barrier coatings: Mixed-mode interfacial fracture toughness and sintering behavior. *Surface & Coating Technology*. 2016; 286: 119-128. Available at: DOI: 10.1016/j.surfcoat.2015.12.012
7. Wang X., Wang C., Atkinson A. Interface fracture toughness in thermal barrier coatings by cross-sectional indentation. *Acta Materialia*. *Acta Materialia Inc.*; 2012; 60(17): 6152–6163. Available at: DOI:10.1016/j.actamat.2012.07.058
8. Krishnasamy J., Ponnusami SA., Turteltaub S., van der Zwaag S. Computational investigation of porosity effects on fracture behavior of thermal barrier coatings. *Ceramics International*. Elsevier Ltd and Techna Group S.r.l.; 2019; 45(16): 20518–20527. Available at: DOI:10.1016/j.ceramint.2019.07.031
9. Kyaw ST., Jones IA., Hyde TH. Simulation of failure of air plasma sprayed thermal barrier coating due to interfacial and bulk cracks using surfacebased cohesive interaction and extended finite element method. *Journal of Strain Analysis for Engineering Design*. 2016; 51(2): 132–143. Available at: DOI:10.1177/0309324715615746
10. Nicholls JR., Jaslier Y., Rickerby DS. Erosion and foreign object damage of thermal barrier coatings. *Materials Science Forum*. 1997; 251– 254(PART 2): 935–948. Available at: DOI:10.4028/www.scientific.net/msf.251-254.935
11. Nicholls, J. R., Jaslier, Y., & Rickerby, D. S. Erosion of EB-PVD thermal barrier coatings. 1998; *Materials at High Temperatures*, 15(1), 15–22. Available at: <https://doi.org/10.1080/09603409.1998.11689572>
12. Nicholls JR., Wellman RG., Deakin MJ. Erosion of thermal barrier coatings. *Materials at High Temperatures*. 2003; 20(2): 207–218. Available at: DOI:10.1179/mht.2003.024

13. Wellman RG., Nicholls JR. Erosion, corrosion and erosion-corrosion of EB PVD thermal barrier coatings. *Tribology International*. 2008; 41(7): 657–662. Available at: DOI:10.1016/j.triboint.2007.10.004
14. Chen X., Wang R., Yao N., Evans AG., Hutchinson JW., Bruce RW. Foreign object damage in a thermal barrier system: Mechanisms and simulations. *Materials Science and Engineering A*. 2003; 352(1–2): 221– 231. Available at: DOI:10.1016/S0921-5093(02)00905-X
15. Watanabe M., Xu T., Levi CG., Gandhi AS., Evans AG. Shear band formation in columnar thermal barrier oxides. *Acta Materialia*. 2005; 53(13): 3765–3773. Available at: DOI:10.1016/j.actamat.2005.04.029
16. Chen X., Hutchinson JW. Particle impact on metal substrates with application to foreign object damage to aircraft engines. *Journey of the Mechanics and Physics of Solids*. 2002; 50: 2669– 2690. Available at: doi.org/10.1016/S0022-5096(02)00022-4
17. Wright JM., Faucett DC., Ayre M. Phenomena of Foreign Object Damage by Spherical Projectiles in EB-PVD Thermal Barrier Coatings of Turbine Airfoils. *Journal of Engines for Gas Turbines Power*. 2014; 136. Available at: DOI:10.1115/1.4027362
18. Wellman RG., Deakin MJ., Nicholls JR. The effect of TBC morphology and aging on the erosion rate of EB-PVD TBCs. *Tribology International*. 2005; 38(9 SPEC. ISS.): 798–804. Available at: DOI:10.1016/j.triboint.2005.02.008
19. Yu, Q. M., Q. He, and F. L. Ning. 'Influence of Interface Morphology on Erosion Failure of Thermal Barrier Coatings'. *Ceramics International* 44, no. 17 (1 December 2018): 21349–57. Available at: <https://doi.org/10.1016/j.ceramint.2018.08.188>.
20. Zhu, W., Y. J. Jin, L. Yang, Z. P. Pi, and Y. C. Zhou. 'Fracture Mechanism Maps for Thermal Barrier Coatings Subjected to Single Foreign Object Impact'. *Wear* 414–415 (15 November 2018): 303–9. Available at: <https://doi.org/10.1016/j.wear.2018.08.020>.
21. Matsuzawa M., Abe M., Horibe S. Strain rate dependence of tensile behavior and environmental effect in zirconia ceramics. *ISIJ International*. 2003; 43(4): 555–563. Available at: DOI:10.2355/isijinternational.43.555
22. Chen X., He MY., Spitsberg I., Fleck NA., Hutchinson JW., Evans AG. Mechanisms governing the high-temperature erosion of thermal barrier coatings.

- Wear. 2004; 256(7–8): 735–746. Available at: DOI:10.1016/S0043-1648(03)00446-0 49
23. G.R. and Cook, W.H. (1983) 'A Constitutive Model and Data for Metals Subjected to Large Strains, High Strain Rates and High Temperature', Proceedings of the 7th International Symposium on Ballistic, 21(1), pp. 541–547.
24. Lankford J., Predebon WW., Staehler JM., Subhash G., Pletka BJ., Anderson CE. The role of plasticity as a limiting factor in the compressive failure of high strength ceramics. *Mechanics of Materials*. 1998; 29(3–4): 205–218. Available at: DOI:10.1016/S0167-6636(98)00023-4
25. Schutze M. Protective oxide scales and their breakdown. WILEY; 1997. Available at: [www.wiley.com/en-gb/Protective+Oxide+Scales+and+Their+Breakdown-p-9780471959045](http://www.wiley.com/en-gb/Protective+Oxide+Scales+and+Their+Breakdown-p-9780471959045)
26. Honite G. Blast Media Data Sheet. Guyson. Available at: <https://www.guyson.co.uk/aftersales/guyson-blast-media/glass-blast-media>. Last accessed 13 Feb 2023.
27. Latella BA., Liu T. High-temperature young's modulus of alumina during sintering. *Journal of the American Ceramic Society*. 2005; 88(3): 773– 776. Available at: DOI:10.1111/j.1551-2916.2005.00082.x
28. Mumm DR., Evans GA. Mechanisms controlling the performance and durability of thermal barrier coatings. *Key Engineering Materials*. 2001; 197: 199–230. Available at: DOI:10.4028/www.scientific.net/kem.197.199
29. Czeppe T., Wierzbinski S. Structure and mechanical properties of NiAl and Ni<sub>3</sub>Al-based alloys. *International Journal of Mechanical Sciences*. 2000; 42(8): 1499–1518. Available at: DOI:10.1016/S0020-7403(99)00087-9
30. Dey GK. Physical metallurgy of nickel aluminides. *Sadhana - Academy 51 Proceedings in Engineering Sciences*. 2003; 28(1–2): 247–262. Available at: DOI:10.1007/BF02717135
31. Fleck, N. A., and Th. Zisis. 'The Erosion of EB-PVD Thermal Barrier Coatings: The Competition between Mechanisms'. *Wear* 268, no. 11 (12 May 2010): 1214–24. <https://doi.org/10.1016/j.wear.2009.12.020>.
32. Benachour M. Effect of the amplitude loading on fatigue crack growth. *Procedia Engineering*. 2010; 2: 121–127.

33. Xing Y., Wei Q., Hao J. The fracture toughness of alumina coatings plasma-sprayed at different in situ temperatures. *Ceramics International* 38 (2012) 4661-4667. Available at: [doi.org/10.1016/j.ceramint.2012.02.048](https://doi.org/10.1016/j.ceramint.2012.02.048)

Journal Pre-proof

**Declaration of interests**

The authors declare that they have no known competing financial interests or personal relationships that could have appeared to influence the work reported in this paper.

The authors declare the following financial interests/personal relationships which may be considered as potential competing interests:

Journal Pre-proof

2023-05-15

# Estimation of thermal barrier coating fracture toughness using integrated computational materials engineering

Geng, Xibo

Elsevier

---

Geng X, Wellman R, Isern Arrom L, et al., (2023) Estimation of thermal barrier coating fracture toughness using integrated computational materials engineering. *Ceramics International*, Available online 15 May 2023

<https://doi.org/10.1016/j.ceramint.2023.05.124>

*Downloaded from Cranfield Library Services E-Repository*